Guided-Mode-Resonance Reflectors for Performance Enhancement of Sapphire Based Fabry-Perot Sensors in Harsh Environment

Wang Jiayan ⓘ, Ma Zhibo, Yuan Xichen, Sun Xu, Tang Luhong, Xi Qi, and Wang Yinan

Abstract—**This paper presents a guided-mode resonance (GMR) reflector for sapphire based Fabry-Perot (F-P) sensors that enables tunable or wideband high reflectance with high temperature resistance, which is expected to effectively regulate the performance of F-P sensors and offer a novel approach for designing F-P sensors in harsh environments. Intrinsic and extrinsic GMR gratings are proposed, and their optical and thermal properties are investigated and compared through numerical simulations, such as rigorous coupled-wave analysis and finite element analysis methods. The quantitative results indicate high feasibility for harsh environment applications and the potential for adopting different demodulation methods. Significant enhancement in the F-P sensor performance is obtained through analysis based on the F-P interference model, and the spectrum fineness and sensor sensitivity can be enhanced by at least one order of magnitude. The GMR reflector can be extended to other types of F-P sensors, demonstrating significant potential in high-temperature applications.**

Index Terms—**Fabry-Perot sensor, guided mode resonance, harsh environment, sapphire.**

I. INTRODUCTION

PRESSURE and acoustic sensing in harsh environments are urgently required in various major industrial fields, particularly in aerospace applications such as gas turbine engines. In situ, real-time measurement of pressure and acoustic signals generated in compressors, combustors, and turbines is one of the most effective approaches for realizing damage prediction, combustion monitoring, and thrust assessment of engines [1]. However, harsh environments with high temperature, pressure, and corrosiveness, especially in the combustor and turbine, require extreme tolerance of the adopted sensor for in-situ measurement, which makes most current electrical sensors unsuitable.

Fiber optic Fabry-Perot (F-P) sensors, particularly extrinsic Fabry-Perot interference sensors (EFPISs), have exhibited broad prospects in harsh environment applications owing to their high sensitivity and potential high temperature resistance caused by the strong variability of the diaphragm material. Numerous efforts have been made to improve the performance of EFPISs in high-temperature applications by utilizing silicon carbide [2], quartz [3], and sapphire-based [4] diaphragms. Among them, sapphire is the most promising material because of its excellent physical and chemical stability, temperature resistance, and optical properties, hence its wide application in fiber optic sensors, especially for pressure sensing [5]–[8].

The performance of EFPIs can be divided into three key parts of signal-mechanic, mechanic-optic and optic-electric, which in turn depend upon the mechanical compliance of the diaphragm, the reflectivity of the diaphragm-air interface, the optical-electricity transfer efficiency of the read-out circuit as well as the demodulation algorithm, the overall performance of EFPIs is relative to all three parts [9]. The signal-mechanic part of sapphire EFPIs is relatively hard to optimize due to the difficulty of fabricating sapphire brought by its extreme hardness and stable chemical property. In contrast, a more feasible alternative for improving the mechanic-optic part may be through regulating the reflectance of sapphire-air interface. Generally, metal reflector membrane is widely used to form a high-reflectance interface in EFPIs [9]–[13], this is beneficial to improving spectrum fineness as well as light-fiber coupling efficiency. However, the thermal stress caused by the heterostructure at high temperatures may break the continuity of the reflector membrane.

Guided mode resonance (GMR) effect, owing the ability of tailoring optical field and reflect spectrum, is proven to be capable of applying in various optical devices such as wideband reflector [14]–[19]. The capability of regulating reflect spectrum also bring significant potential for application in F-P sensor [20], [21]. Aiming for the widely adopted demodulation methods of F-P sensor such as light intensity based [10]–[13] or phase based [22]–[24] method, a carefully designed GMR is capable to provide most suitable spectrum. Meanwhile, GMR grating is expected to exhibit higher temperature resistance than metal reflector for the absence of continuous hetero layer. Therefore, it is believed that GMR grating is a promising technique for property enhancement of sapphire based EFPIS.

In this paper, GMR gratings are proposed to optimize the performance of sapphire based Fabry-Perot sensor, the GMR

The authors are with The Ministry of Education Key Lab of Micro/Nano System for Aerospace, Northwestern Polytechnical University, Xi'an 710072, China, and also with the Shaan'xi Key Lab of MEMS/NEMS, Northwestern Polytechnical University, Xi'an 710072, China (e-mail: wangjiayan@mail.nwpu.edu.cn; zbma@nwpu.edu.cn; xichen.yuan @nwpu.edu.cn; sunxu@nwpu.edu.cn; tangluhong@mail.nwpu.edu.cn; qqxiqi001@mail.nwpu.edu.cn; wangyinan@mail.nwpu.edu.cn).
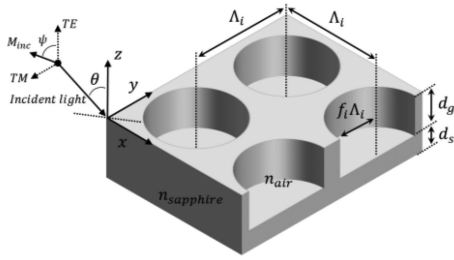
Fig. 1. Model of periodic structures in intrinsic GMR reflector. Λ_i, f_i, d_g, d_s are the period, fill factors, thickness of grating layer, and substrate layer, respectively. M_{inc} describes the magnetic component of the incident light while ψ and θ denotes its incidence and polarization angle. $n_{sapphire}$ and n_{air} are the refractive indexes of sapphire and air and are 1.745 [25] and 1, respectively.

gratings are divided into intrinsic and extrinsic type. For the two types of GMR grating, both wideband reflector and narrow band filter waveforms are separately realized based on their physical mechanisms. The parameters of the GMR grating are obtained through the particle swarm optimization (PSO) algorithm with rigorous-coupled-wave analysis (RCWA) as the kernel, and the results are confirmed by comparing those calculated by both finite element analysis (FEA) and RCWA methods. Furthermore, the influence of high temperature on GMR performance has been investigated through numerical simulations, which further supports the discussion on the applicability of these two types of GMR. In conclusion, a novel approach is proposed to improve the performance of a sapphire based EFPIs, which shows broad prospects for a wide range of high-temperature sensor applications.

II. PROPOSED GMR REFLECTOR AND DESIGN METHOD

A. Intrinsic GMR Reflector

The proposed intrinsic GMR reflector without the hetero layer is shown in Fig. 1. The overall structure consists of a grating layer with width d_g and a substrate layer with width d_s, while a square array of air holes with period Λ_i and fill factor f_i (ratio of hole radius to period) is constructed on the grating layer. Given that multiple optical modes are likely to exist in practical applications, the reflector is designed to be centrosymmetric to ensure the necessary polarization independence for potential adaption.

The current design was chosen considering the relative difficulty in forming a wideband reflectance using sapphire because of its low refractive index, and as the width of the high-reflectance band may be broadened through the introduction of a sublayer [15], [18]. The increased degree of freedom in design is also beneficial for obtaining a spectrum with multiple characterizations.

B. Extrinsic GMR Reflector

To enhance the versatility of our device and supplement the limitations of the intrinsic GMR reflector caused by a low refractive index, an extrinsic GMR reflector with scatters is proposed. Compared with the intrinsic GMR reflector, the overall structure is simplified and consists of only periodic scatters and a sapphire substrate; therefore, the input parameters for
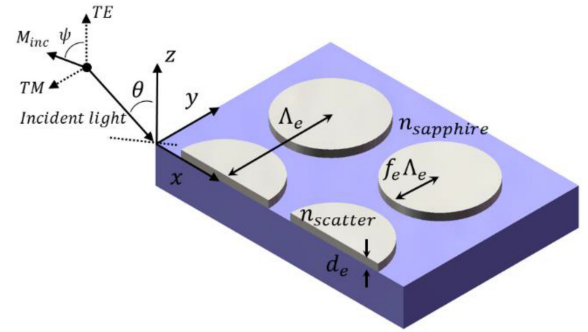

Fig. 2. Model of periodic structures in sapphire-based extrinsic GMR reflector. Λ_e, f_e, d_e, are respectively period, fill factor, thickness of grating layer and substrate layer. $n_{sapphire}$ and $n_{scatter}$ denotes the refractive index of sapphire and scatter respectively.

PSO can be reduced' to three parts: period of scatter array Λ_e, fill factor f_e(scatter radius/period), and thickness of scatter d_e, as displayed in Fig. 2. Moreover, the optical property of the extrinsic GMR reflector is mainly manipulated by scatters on the sapphire substrate, which eliminates the demand for substrate thickness and significantly increases the applicability in realizing GMR grating.

Herein monocrystalline silicon is chosen to make scatters considering that silicon based micro fabrication is mature thus bring in convenience in manufacturing scatters. Moreover, silicon has a relatively high refractive index at $\lambda = 1.55\mu m$ ($n_{Mono-Si} = 3.48$ [26]), which is essential to form a strong resonance mode to manipulate the optical property of scatter.

C. Design Method

A particle swarm optimization (PSO) algorithm associated with rigorous-coupled-wave-analysis (RCWA) has been utilized to search for suitable parameters of GMR gratings, which is a robust and readily adopted strategy for GMR grating design [17]. The numerical method to calculate reflectance is based on RCWA, which constructs a fuzzy mapping between grating parameters and reflectivity and can be used to invert parameters based on target reflectivity. The whole flow of designing GMR reflector is exhibited in Fig. 3. The particles are firstly initialized with positions and velocities in parameter searching space, the searching space is set according to the type of grating and the expected geometric size, as given in Table I. Subsequently, the fitness function of each particle is calculated, the globally optimal value is selected and then used to estimate whether the loop is end or not. Here, the position of particle stands a set of grating parameters in the searching space, the reflectance and fitness function of this set is obtained by RCWA, therefore RCWA functions as a feedback kernel. The loop stops when reaching maximum iterations (500 iterations set in our calculation), or the fitness function achieve its threshold (1×10^{-10} in our calculation).

In our case, considering the target of the wideband flat-top reflector (WFR) and tunable-reflectance reflector (TRR), the fitness function of the PSO is respectively given in equation (1) and (2) as follow. Moreover, the working waveband is set to be $1.45\mu m - 1.65\mu m$ considering that the dimension of

TABLE I
PARAMETERS SEARCHING SPACE OF GMR GRATING

Reflector type\GMR type	Intrinsic	Extrinsic
TRR (μm)	Λ_i [0.001,2] f_i [0.01,0.49] d_g [0.001,2] d_s [0.001,2]	Λ_e [0.001,1] f_e [0.01,0.49] d_e [0.001,1]
WFR (μm)	Λ_i [0.001,2] f_i [0.01,0.49] d_g [0.001,2] d_s [0.001,2]	Λ_e [0.001,1] f_e [0.01,0.49] d_e [0.001,0.5]

TABLE II
PARAMETERS OF GRATING

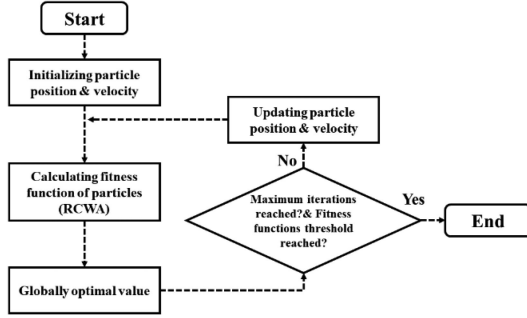| Reflector type\GMR type	Intrinsic	Extrinsic
TRR	$\Lambda_i = 1.250\mu m,$ $f_i = 0.389,$ $d_g = 0.522\mu m,$ $d_s = 0\mu m$	$\Lambda_e = 0.721\mu m,$ $f_e = 0.380,$ $d_e = 0.474\mu m$
WFR	$\Lambda_i = 1.463\mu m,$ $f_i = 0.420,$ $d_g = 1.071\mu m,$ $d_s = 0.605\mu m$	$\Lambda_e = 0.692\mu m,$ $f_e = 0.357,$ $d_e = 0.462\mu m$

Fig. 3. Flow chart of the PSO algorithm used in designing GMR reflector.

the GMR cell is similar to its objective wavelength, and thus a relatively large wavelength would significantly enhance the feasibility of fabrication by increasing the minimum linewidth in micro-fabrication. Meanwhile, the dispersion and birefringence of sapphire is ignored during calculation, which is expected to simplify the analyze model and saving the time consumption for subsequent investigation, corresponding verification supporting this setting can be found in following chapter. Therefore, only the refractive index at $\lambda = 1.55\mu m$ is used in the calculation.

Generally, wideband reflectance is formed by a single resonance mode that exists in a wide waveband or several resonant modes closely adjacent in the wavelength domain [15]–[19], therefore the reflectance could be nearly 100% over a wide range. Accordingly, the fitness function is defined as a root-mean-square-type equation as follows:

$$F = \sqrt{\frac{1}{N}\sum_{i=1}^{N}[1 - R_c(\lambda_i)]^2} \qquad (1)$$

where 1 is the expected zero-order reflectance, $R_c(\lambda)$ is the counterpart in PSO calculated by RCWA, N is the number of discrete points, and λ_i is the discrete wavelength point in the working waveband.

On the other hand, tunable-reflectance can be realized as long as a rising or falling edge exists; therefore, several mechanisms could be used to create a TRR, such as a sharp peak in the spectrum inspired by the resonance of a specific wavelength [27], [28]. Meanwhile, the width and location of the edge are not considered because it is relatively complicated to describe

an edge mathematically; therefore, the fitness function for designing the TRR is defined as

$$F = 1 - max\left(R_c\left(\lambda_{i = 1...N}\right)\right) + min\left(R_c\left(\lambda_{i = 1...N}\right)\right) \quad (2)$$

where $max(R_c(\lambda_{i = 1...N}))$ and $min(R_c(\lambda_{i = 1...N}))$ represent the maximum and minimum reflectance in every optimization loop during the PSO calculation. The equation is not a rigorous definition of rising/falling edges, and the result of the PSO cannot be fixed uniquely. However, for the guided mode, resonance always leads to a sharp peak with an amplitude close to 100%, as we know; thus, a rising/falling edge can be expected to exist in the objective spectrum after several optimizations.

III. OPTICAL SIMULATION

Table II displays the parameters of both the wideband and narrow band reflectors of the intrinsic/extrinsic GMR gratings calculated by PSO.

To verify the correctness of our design method and the assumption that dispersion and birefringence of sapphire can be ignored during calculation. Intrinsic WFR is taken as example, the spectrum is calculated by FEA & RCWA, refractive index with dispersion and with birefringence of sapphire.

As shown in Fig. 4, the results calculated by different methods and refractive models demonstrate close agreement but with a small deviation of approximately several nanometers overall shift.

For Fig. 4(a), this might be caused by several factors which are not related to the structure, such as meshing imprecision and numerical truncation error in different calculation methods in RCWA and FEA methods.

For Fig. 4(b), refractive constrast is known as the main factor that affect the property of GMR reflector, the difference between our applied refractive index ($n_{sapphire} = 1.745$) and those given by previous work with dispersion [29] is only 0.01%–0.5%, therefore we believe it is the small quantity of refractive contrast difference that leads to two similar spectrums.

As for birefringence of sapphire, according to [30], and given that z-axis of GMR reflector is set as the c-axis of sapphire, the refractive index is reconsidered defined as a diagonal matrix with diagonal line of $[n_e\ n_e\ n_o]$, where $n_o = 1.745$ ($\lambda = 1.55\mu m$) stands the refractive index of ordinary light and $n_e = 1.738$ ($\lambda = 1.55\mu m$) represents the refractive index of extraodinary
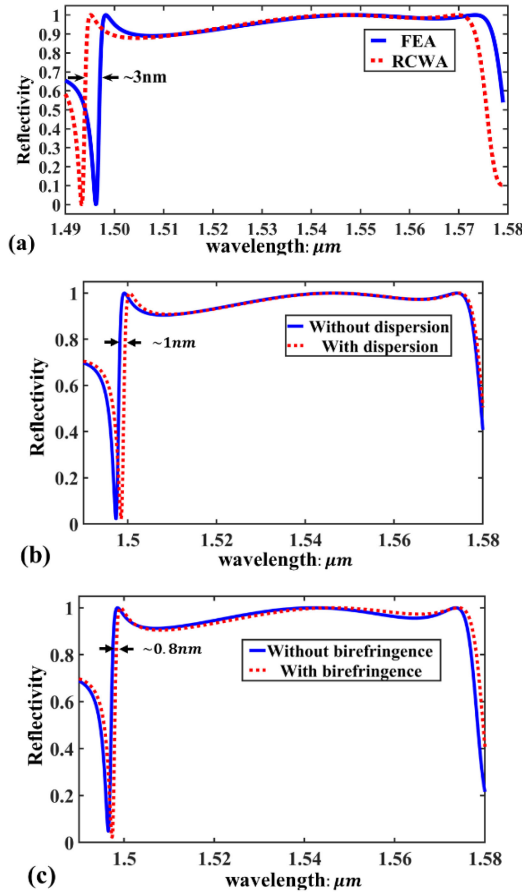
Fig. 4. Reflectance spectrum of sapphire based intrinsic GMR grating calculated by (a) RCWA and FEA, (b) Refractive index with dispersion and without dispersion, (c) Refractive index with birefringence and without birefringence. Where the incident angle $\theta = 0°$ and the polarization angle $\psi = 90°$ (TM polarization).

light propagating through directions perpendicular to c-axis. The difference of n_o and n_e leads to two spectrums with same extent but with an overall shift of only $0.8nm$, shown in Fig. 4(c).

Based on Fig. 4, we can conclude that the design of our GMR reflector is effective, and the refractive index can be simplified as a constant value without considering the dispersion and birefringence, which will significantly reduce the complexity of model and save time consumption for following analysis.

Following, the reflectance spectra of all types of GMR gratings are calculated through FEA, and the mechanisms of both extrinsic and intrinsic reflectors are discussed, as shown in Figs. 5, 6 and 7. It is worth mentioning that previous efforts have been made on multiple decomposition in analyzing the optical properties of similar scatters [31], which can be used to investigate the underlying mechanism of our GMR grating. Herein, we focus on the design and application of GMR grating, and so present only a simplified explanation in the following discussion as opposed to a rigorous mathematical model.

A. Intrinsic GMR Reflector

A preliminary description of the optical properties of the intrinsic WFR can be found in Fig. 4, a band of $R > 0.85$ in the range of $1.495\mu m$ to $1.573\mu m$ across $78nm$ exists in the
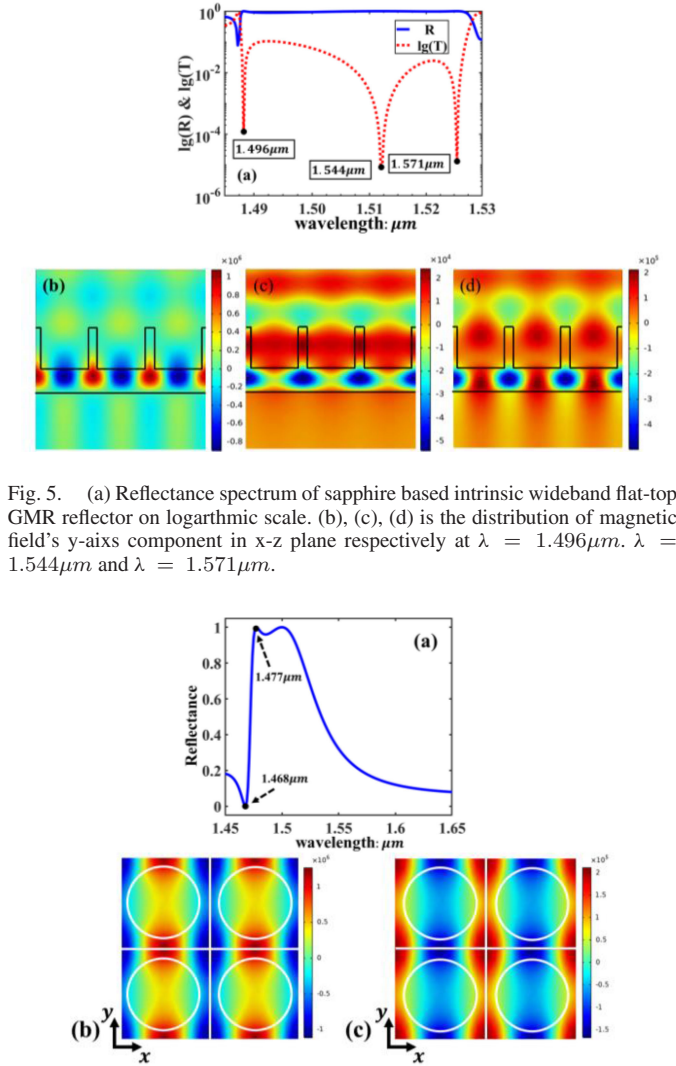

Fig. 5. (a) Reflectance spectrum of sapphire based intrinsic wideband flat-top GMR reflector on logarthmic scale. (b), (c), (d) is the distribution of magnetic field's y-aixs component in x-z plane respectively at $\lambda = 1.496\mu m$. $\lambda = 1.544\mu m$ and $\lambda = 1.571\mu m$.
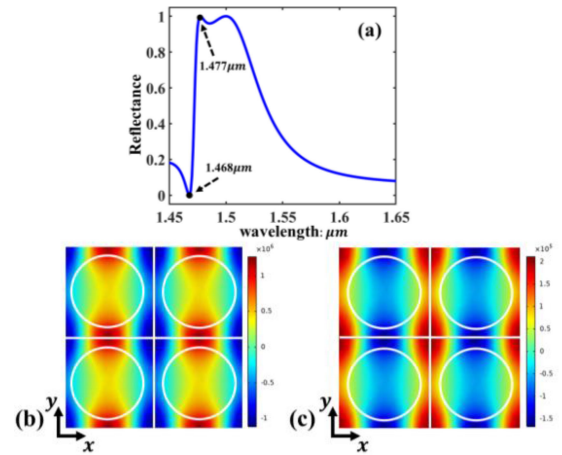

Fig. 6. (a) Reflectance spectrum of sapphire based intrinsic tunable-reflectance GMR reflector. (b) and (c) indicate the distribution of the magnetic field's y-axis component in the x-y plane respectively at the trough $\lambda = 1.468\mu m$ and peak $\lambda = 1.477\mu m$.
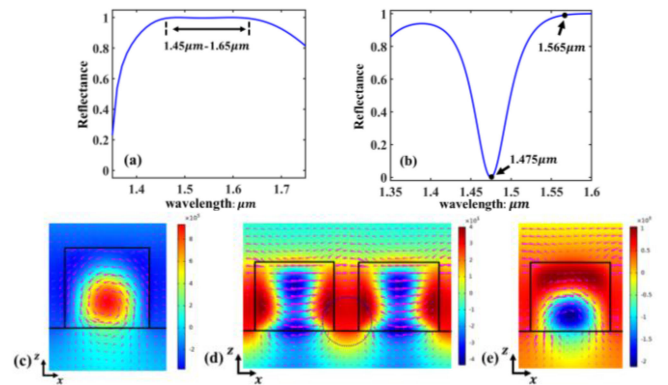

Fig. 7. Optical property of extrinsic GMR grating simulated through FEA. (a) and (b) indicate the reflectance spectrum of WFR and TRR simulated by FEA. (c), (d) and (e) show the distribution of the magnetic field's y-axis component in the x-z profile of WFR and TRR scatter, respectively at $\lambda = 1.55\mu m$, $\lambda = 1.475\mu m$ and $\lambda = 1.565\mu m$, where pink cones indicate the vector of displacement current, and the size of the cone is propotional to the current amplitude.

spectrum. To investigate the formation of this wideband reflection, the corresponding reflectance and transmittance spectra are displayed on a logarithmic scale, which magnifies the fluctuation in the spectrum and helps to identify the latent resonance peaks [16], [17], as shown in Fig. 5(a).

As shown in Fig. 5(a), there are three troughs inside the transmittance spectrum, each indicating a guided-mode resonance, located at $\lambda = 1.496\mu m$, $\lambda = 1.544\mu m$, and $\lambda = 1.571\mu m$. Furthermore, the band is much less flat than the extrinsic wideband flat-top GMR reflector with scatters, which is assumed to be because the refractive index of sapphire is much lower than that of monocrystalline silicon, which leads to less efficiency in confining light and forming resonance. Another feasible explanation is that the band of the intrinsic GMR reflector resulted from the co-existence and interaction of the three guided mode resonances, while the band of the extrinsic GMR reflector is caused by a single strong resonance mode.

For further consideration of the formation of this reflection band, the internal magnetic field distribution in the intrinsic wideband flat-top GMR reflector is shown in Fig. 5(b)-(d) at $\lambda = 1.496\mu m$, $\lambda = 1.544\mu m$, and $\lambda = 1.571\mu m$. According to the pattern, it may be assumed that the resonance is generated via coupling of evanescent diffraction waves and a leaky mode supported by the grating, which in turn forms a standing wave pattern; these leaky mode resonances form independent troughs in the transmittance spectrum and further result in a high reflectance band located in the range of $1.495\mu m$ to $1.573\mu m$.

The spectrum of the intrinsic TRR is shown in Fig. 6(a), where a rising edge across $1.468\mu m$-$1.477\mu m$ is found in the spectrum, and the variation of reflectance of this edge ranges from 0.1% to 99.9%. According to previous studies of dielectric GMR gratings, the spectrum is assumed to be formed by the co-existence of two closely distributed resonances and a Fano resonance is responsible for the sharp rising edge we're looking for [31], [32]. Furthermore, considering that the high refractive index part of the tunable-reflectance intrinsic GMR reflector is continuous, the distribution of the magnetic field on the x-y profile is given to help further discussion, as shown in Fig. 6(b)–(c).

As can be seen, the resonance patterns of $\lambda = 1.468\mu m$ and $\lambda = 1.477\mu m$ indicate similar trends of distribution along the y-axis, but an obvious difference in the distribution along the x-axis. In other words, the guided mode supported by the grating at $\lambda = 1.468\mu m$ and $\lambda = 1.477\mu m$ exhibits a difference in phase along the x-axis, forming destructive interference and constructive interference with incident light, respectively, resulting in the trough and peak in the spectrum.

B. Extrinsic GMR Reflector

As for extrinsic WFR, Fig. 7(a) shows a flat top reflectance spectrum across $1.45\mu m - 1.65\mu m$ formed by our optimized grating parameters. The underlying physical mechanism is assumed to be a magnetic dipole resonance generated by eddy displacement current in the scatter, which forms a strong resonance and causes the wide, flat-top band [30]. The mechanism of $\lambda = 1.55\mu m$ is displayed in Fig. 7(c), note that the distribution

of magnetic field at other wavepoints in the flat-top band exhibits same pattern.

As for extrinsic TRR, a peak with a rising edge across $1.475\mu m - 1.565\mu m$ appears in the reflectance spectrum, as shown in Fig. 7(b). To investigate the mechanism behind this, the distribution of the magnetic field located at $\lambda = 1.475\mu m$ and $\lambda = 1.565\mu m$ was obtained and compared, as shown in Fig. 7(d) and Fig. 7(e). The most significant distinction between the two patterns is that the magnetic fields of the scatterers are coupled with each other in the case of $\lambda = 1.475\mu m$, which can be further confirmed by the area indicated by the blue circle in Fig. 7(d), where the displacement current passes through the adjacent scatters and then forms an eddy current. On the other hand, the magnetic field is confined in the scatter in the case of $\lambda = 1.565\mu m$, and $\lambda = 1.565\mu m$ is also speculated to be the starting point of a high reflectance band considering the shape of the spectrum. Moreover, the underlying mechanism of the high reflectance band is considered to be a weak magnetic dipole resonance according to the distribution and amplitude of the magnetic field, as well as the spatial location of the displacement current, as shown in Fig. 7(e). In conclusion, the trough in the spectrum is caused by a resonance mode that occurs when there is a coupling effect between adjacent scatters. Considering the spectrum, it is also reasonable to believe that this type of resonance can only be produced by incident light of a specific wavelength. It is also worth mentioning that other factors such as resonance motivated by high-order multiples can also bring troughs or apexes in the spectrum, whereas here we only discuss the mechanism of the reflector with one set of calculated parameters.

IV. TEMPERATURE INFLUENCE ON OPTICAL PROPERTY

In order to investigate the applicability of our proposed GMR device, the temperature resistance was theoretically investigated. Herein, the transformation of the optical properties of GMR in high-temperature environments is mainly attributed to the thermal expansion effect (TEE) and the temperature effect of refractive index (TERI) of the grating. The thermal expansion model of intrinsic and extrinsic GMR gratings is discussed separately in the subsequent chapter, owing to their different mechanical constraints. However, the effect of temperature on the refractive index should be the same for both types of gratings. Generally, refractive index is described as a function of wavelength and temperature, however, the dispersion of both sapphire and silicon is extremely low in the infrared waveband [25], [26], therefore the refractive index of $\lambda = 1.55\mu m$ is utilized in calculation. In addition, the refractive index with respect to temperature is given as,

$$n_T = n_0 + \sigma (T - T_0) \tag{3}$$

Where n_T, n_0 is the refractive index at the current temperature and initial temperature, respectively, σ is the thermal-optic coefficient of the refractive index, the values of sapphire and silicon are used according to previous studies [33], [34], T and T_0 are the current and initial temperatures, respectively. Note that the TERI of air is not considered because of its extremely

TABLE III
LOCATION AND REFLECTANCE OF SAMPLING POINTS FOR INTRINSIC
REFLECTOR

Temperature	WFR Point1/Point2	TRR Point1/Point2
298 K	$1.497\mu m, 98.74\%$ $1.545\mu m, 100\%$	$1.469\mu m, 0.01\%$ $1.479\mu m, 99.99\%$
698 K	$1.501\mu m, 99.10\%$ $1.550\mu m, 100\%$	$1.476\mu m, 0.03\%$ $1.486\mu m, 100\%$
1098 K	$1.507\mu m\ 98.90\%$ $1.555\mu m, 100\%$	$1.483\mu m, 0.16\%$ $1.493\mu m, 100\%$
1498 K	$1.512\mu m\ 99.67\%$ $1.560\mu m, 100\%$	$1.489\mu m, 0.001\%$ $1.500\mu m, 99.97\%$
1898 K	$1.517\mu m, 99.93\%$ $1.566\mu m, 100\%$	$1.495\mu m, 0.004\%$ $1.506\mu m, 100\%$

low σ, thus formula (3) is related only to sapphire in the case of an intrinsic GMR reflector but should be utilized twice for both sapphire and scatter in the case of an extrinsic GMR reflector.

A. Intrinsic GMR Reflector

In the case of an intrinsic GMR reflector, the TEE of the entire GMR grating is simplified to a linear combination of single GMR cells in Cartesian coordinates with only linear TEE, and a single GMR cell can be chosen as the research objective. According to previous research on the properties of sapphire, the coefficients of thermal conductivity, thermal expansion, and thermal diffusion [35] are imported into an FEA-based analysis model to obtain the swell increment along each axis. The overall process of the simulation is shown in Fig. 8(a), which presents two main steps of thermal analysis and optical simulation based on the reconstructed geometry of the grating. Note that the parameters mentioned above are described as a second-order tensor because of the anisotropy of sapphire; thus, the expansion is not the same along every axis.

The external temperature of the grating was set to be $298 - 1898\ K$ with $400\ K$ as the interval to investigate the influence of temperature on the intrinsic GMR grating. As shown in Fig. 8(d) and (e), both reflectors' reflection spectra show a similar extent of redshift without changing the spectrum shape in the whole spectrum. To quantify the influence of temperature on the reflection spectrum, two points located at the peak and valley of the spectrum and both sides of the high-reflectance band are chosen for the TRR and WFR, as marked in Fig. 8(d) and (e). The reflection and wavelength of these points at different external temperatures are listed in Table III. It is clear that the redshift of the whole spectrum, and the amplitude of this redshift, are approximately proportional to the temperature variation with ratios of approximately $0.015\ nm/K$ and $0.0175\ nm/K$ for WFR and TRR, respectively. In conclusion, according to our calculation only a linear offset of the spectrum occurs as the temperature increases. Thus, the intrinsic GMR grating is expected to be theoretically effective for the linear offset of the spectrum, which can be easily compensated for by shifting the waveband in the demodulation process.
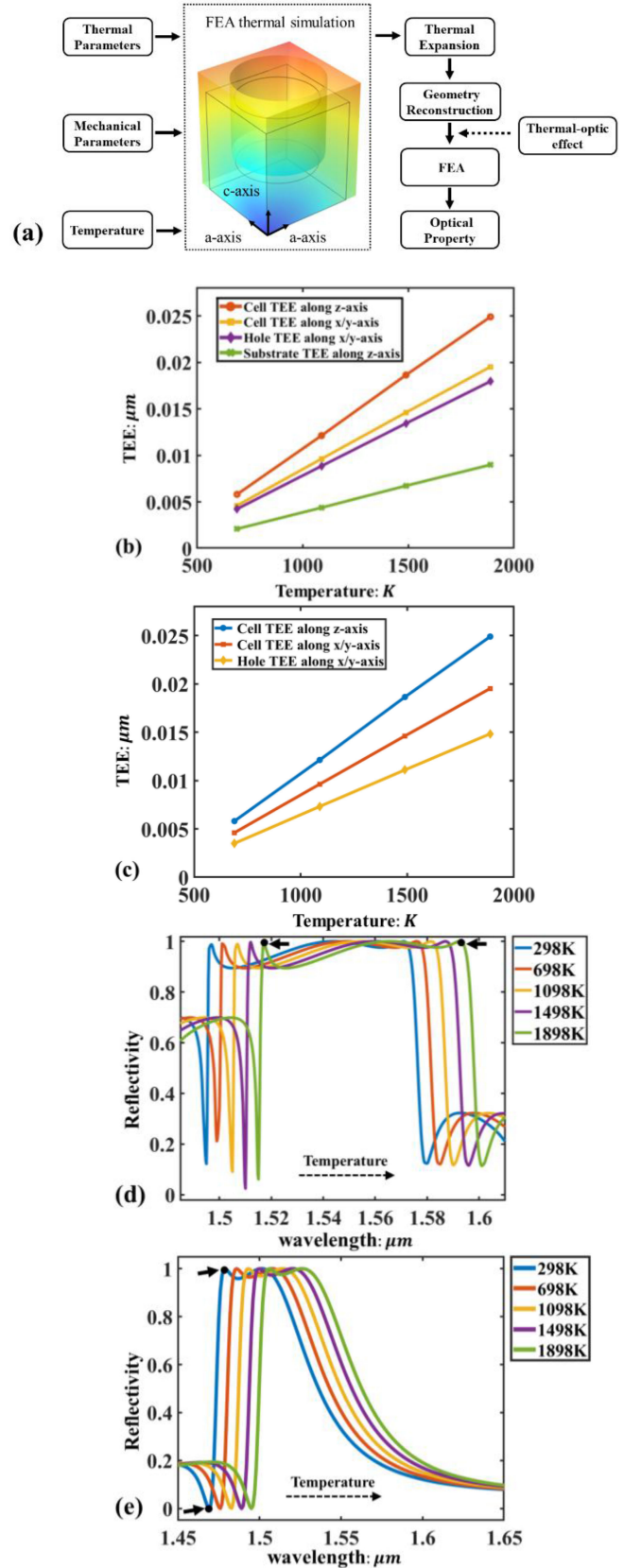

Fig. 8. (a) flow diagram of the thermal analysis process. (b) and (c) give the TEE data to reconstruct geometry of intrinsic WFR and TRR. (d) and (e) indicate the reflection spectrum of intrinsic WFR and TRR grating at different external temperature, black points and arrows indicate the chosen sampling points.

Temperature	WFR	TRR
	Point1/Point2	Point1/Point2
298K	$1.425\mu m, 94.94\%$	$1.475, 0.39\%$
	$1.685\mu m, 94.92\%$	$1.5084, 70.10\%$
498K	$1.425\mu m, 95.02\%$	$1.475\mu m, 0.37\%$
	$1.685\mu m, 95.02\%$	$1.5087\mu m, 70.14\%$
698K	$1.425\mu m\ 95.13\%$	$1.475\mu m, 0.41\%$
	$1.690\mu m, 94.80\%$	$1.5087\mu m, 70.09\%$
898K	$1.425\mu m\ 95.27\%$	$1.475\mu m, 0.38\%$
	$1.690\mu m, 94.93\%$	$1.5089\mu m, 70.01\%$
1098K	$1.425\mu m, 95.39\%$	$1.475\mu m, 0.42\%$
	$1.695\mu m, 94.62\%$	$1.5092\mu m, 70.25\%$
1298K	$1.425\mu m, 95.46\%$	$1.475\mu m, 0.41\%$
	$1.695\mu m, 94.71\%$	$1.5094\mu m, 70.32\%$

B. Extrinsic GMR Reflector

In the case of an extrinsic GMR reflector, the thermal analysis process is similar to that of the intrinsic GMR grating, and a cell with a single scatter was chosen as the objective. However, the nonlinear effect cannot be ignored because of the tight mechanical constraint brought by the scatter-substrate interface, which leads to nonlinear thermal expansion of scatter. Meanwhile, the thermal stress brought by the hetero interface was also calculated to evaluate the temperature resistance of the scatter. Previous studies on the thermal properties of silicon have provided its coefficient of thermal conductivity [36], thermal expansion [37], and thermal diffusion [36], [38]; herein, these parameters are imported to FEA to obtain the thermal expansion and stress of scatter. Meanwhile, the temperature influence on refractive index of silicon is also considered, and the coefficient of refractive index versus temperature is selected according to Jellison *et al.* [34]. The adjusted thermal analysis process is shown in Fig. 9(a).

For thermal stress analysis, to the best of our knowledge no previous effort has been made to measure the bonding strength of a silicon membrane on a sapphire substrate; thus, herein we provide only the calculation result of thermal stress for a preliminary evaluation, as shown in Fig. 9(b). The magnitude of the thermal stress at the scatter-substrate interface is approximately linear with the temperature variation, and reaches approximately $3\ GPa$ at $1298\ K$. Detailed thermal stress data are shown in Table IV.

For the optical property, the thermal expansion of the scatter is first obtained through FEA. Herein, the external temperature loaded on the extrinsic grating is set to be $298K - 1298K$ with $200K$ as the interval. The thermal expansion of the scatter is assumed to be nonuniform along the z-axis because the bottom of the scatter is tightly bonded to the substrate, while the top of the scatter is free, and the coefficient of thermal expansion (CTE) of sapphire is higher than that of silicon; therefore, the cylindrical scatter should become a shortened cone as the external temperature rises. This is demonstrated by Fig. 9(c) and (d), wherein the expansion of scatter at the bottom is slightly faster than at the top, and the height of scatter decreases. Subsequently,

the reflectance spectrum is calculated based on the reconstructed geometry of scatter and the adjusted refractive index according to the thermal-optic effect of silicon [35], as shown in Fig. 9(e) and (g). The detailed data of the location and reflectance of the marked points in Fig. 9(e) and (g) can be found in Table IV, where the reflectance at the end point of the TRR is chosen to be approximately 70% for convenient display. The entire spectrum of extrinsic WFR and TRR shifts slightly toward the infrared waveband, and the ratio of redshift versus temperature variation can be calculated as $0.0125nm/K$ and $0.0015nm/K$, respectively, which is the maximum value chosen from several ratios for the offsets that are nonlinear to temperature variation. The amplitude of the red shift is significantly smaller than that of the intrinsic reflector, which can be attributed to the lower thermal expansion for the extrinsic scatter dimension being much smaller than that of the intrinsic reflector, as can be seen in Fig. 8(b) and (c), and Fig. 9(c) and (d). Meanwhile, as shown in Fig. 9(h), the offset is not linear with the variation in temperature, which also verifies the assumption that the thermal expansion of the scatter is nonlinear.

In conclusion, the temperature resistance of the extrinsic GMR grating is apparently lower than that of the intrinsic GMR grating owing to the thermal stress caused by the hetero layer and the low melting point of the scatter material. Additionally, the temperature-induced optical property degeneration of the extrinsic reflector is significantly lower than that of the intrinsic reflector, which indicates a better temperature resistance.

V. APPLICABILITY ON F-P SENSOR

A. Sensor Architecture

Our proposed GMR reflector can be easily integrated into sapphire-based F-P sensors, especially the extrinsic F-P sensor, as shown in Fig. 10, which displays a schematic view of our proposed GMR reflector applied to a typical sapphire-based FFPI pressure sensor. The GMR structure should be fabricated on a small area of the diaphragm in order to decrease the influence on the diaphragm's mechanical properties, whereas the area should also be at least $2 \sim 3$ times larger than the spot size to effectively activate the GMR reflector. Moreover, a collimator with a large focal length is necessary for the optical path of the sensor, considering that most of the commercial lasers can only generate a Gaussian beam, which may invalidate the GMR reflector, and as a Gaussian beam can be transformed to a quasi-plane wave when passing through a collimator with a large focal length.

Correspondingly, fabrication approaches related to EFPIs mentioned above are given below. For intrinsic GMR reflector, two sapphire wafers are firstly sputtered with a nanometer gold layer and then bonded through thermocompression technique, as shown in Fig. 11(a). One of the bonded wafers is then lapped to desired thickness using sapphire CMP lapping technique [39], here the other sapphire wafer functions as a support substrate, as shown in Fig. 11(b). Subsequently, an area is pre-etched to the design thickness, then intrinsic GMR reflector structure is patterned and formed through e-beam lithography and sapphire ICP etching [40], as shown in Fig. 11(c)-(d). Finally, wafer is cut to small pieces by laser, and then the temporary bonding layer is
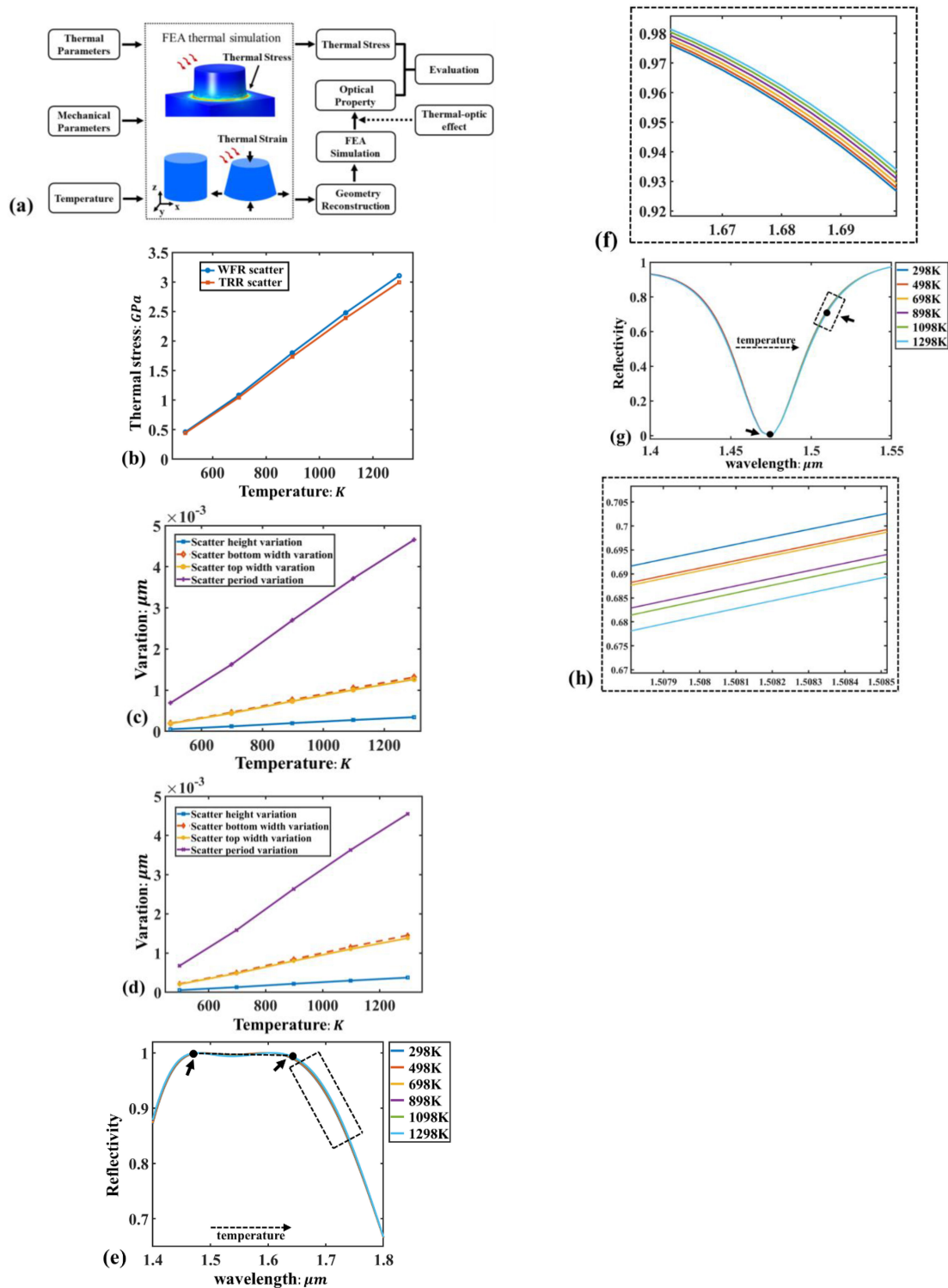
Fig. 9. (a) Flow diagram of the thermal analysis process for extrinsic GMR grating. (c) and (d) give the variation data to reconstruct the geometry of the scatter for WFR and TRR at different external temperatures, respectively; note that the height variation of scatter is along the -z direction, therefore the scatter is shortened as temperature grows. (e) and (g) indicate the corresponding reflection spectrums, where black points and arrows are the chosen sampling points. (f), (h) respectively gives the zoom in view of zone marked with black dashed rectangular in (e) and (g).

moved through chemical etching and the fabricated diaphragm with GMR reflector is bonded to a substrate by epoxy to form sensor head, as exhibited in Fig. 11(e)-(f).

For extrinsic GMR reflector, a commercial silicon-on-sapphire (SOS) wafer is lapped to designed thickness through

sapphire side, given in Fig. 12(a)-(b). Subsequently, e-beam lithography and silicon ICP etching techniques are used to form scatters array pattern, as shown in Fig. 12(c)-(d). Finally, the wafer is cut to small wafers and furtherly bonded to substrate by epoxy to form sensor head.
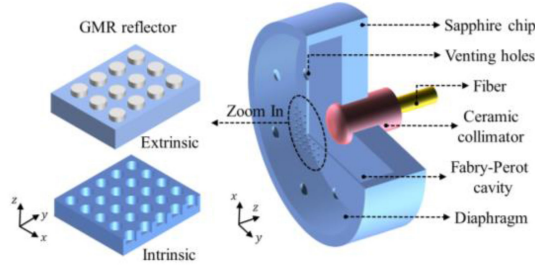
Fig. 10. Schematic view of sapphire-based GMR reflector applicated on a typical EFPI pressure sensor.
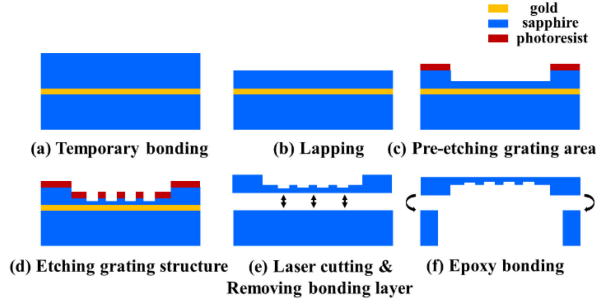

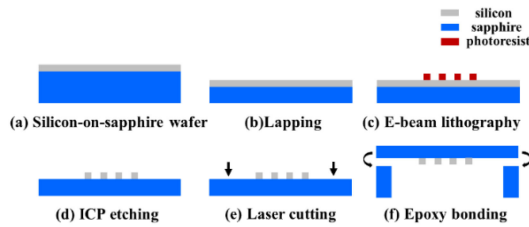Fig. 11. Fabrication flow of EFPIS integrated with intrinsic GMR reflector.

Fig. 12. Fabrication flow of EFPIS integrated with extrinsic GMR reflector.

B. Fabry-Perot Interference Spectrum Regulation

According to the sensor architecture shown above, an F-P interference model combined with a Gaussian beam model is applied to evaluate the result of utilizing the GMR grating in the F-P sensor.

$$I_r(L) == \int_0^a A \frac{2\pi I_0 r}{w_0^2} exp\left(-\frac{2r^2}{w_0^2}\right) dr \quad (4)$$

$$A = \frac{R_1 + R_2 + 2\sqrt{R_1 R_2}\cos(\varphi)}{1 + R_1 R_2 + 2\sqrt{R_1 R_2}\cos(\varphi)}, \quad \varphi = \frac{4\pi n L}{\lambda} \quad (5)$$

Equation (4) is an approximate expression of the Gaussian beam, where a is the radius of the fiber; I_0 is the light intensity in the center of the spot; A is a coefficient corresponding to the F-P interference as shown in equation (5); R_1 and R_2 are the reflectivity of the mirrors forming F-P interference; and n, L, λ indicate the refractive index, cavity length, and wavelength of incident light, respectively. The spot radius is considered as a constant, w_0, considering that a Gaussian beam can be approximated as a plane wave when passing through a collimator with a large focal length, and the variation of the spot radius can be ignored in this case.

TABLE V
$'(L_0)$ AND DYNAMIC RANGE OF THE F-P SENSOR UTILIZING TUNABLE-REFLECTANCE GMR GRATING AND METAL REFLECTOR

Reflectivity		$A'(L_0)$	Dynamic range
TRR	$R_2 = 0.3$	0.035	118nm
	$R_2 = 0.6$	0.189	53nm
	$R_2 = 0.9$	3.556	13nm
Metal reflector		64.603	6nm

Equations (4) and (5) can be used to quantitatively predict the F-P spectrum of our case, where only A is calculated and $4\pi nnL/\lambda$ is varied from 0 to 2π during the calculation to obtain a spectrum with a complete period. Furthermore, the phase change of reflected light caused by the GMR effect is not considered in our calculation because previous works have proved that the phase change is constant; thus, the phase can be compensated by measurement and shows no influence on the theoretical analysis.

C. Intensity Based Demodulation Method

The intensity-based demodulation method is widely adopted in F-P sensors, which require no large dynamic range but high sensitivity, such as in acoustic sensors. However, the sensitivity and dynamic range of the sensor are mutually restricted because the linear range of the spectrum decreases as the fineness increases. In this case, the proposed tunable-reflectance GMR grating is highly suitable for obtaining the optimized dynamic range and sensitivity by tuning the reflectance.

Here, the sensitivity can be partitioned into three series-wound stages, including pressure-mechanical sensitivity, mechanical-optical sensitivity, and optical-electrical sensitivity, which is similar to the model illustrated by Hunt *et al.* [9]. Therefore, the mechanical-optical sensitivity (S_{MO}) is strictly related to the reflectivity of the mirrors forming F-P interference and can be expressed as

$$S_{MO} = \frac{dI_r(L)}{dL} = I_r'(L_0) = \alpha A'(L_0) \quad (6)$$

where α is an equivalent coefficient replacing the complex expression of equation (5), and L_0 indicates the initial cavity length of the F-P cavity. Only $A'(L_0)$ was calculated to evaluate the enhancement of sensitivity by utilizing the GMR reflector.

The end face of the fiber is assumed to be coated by a metal reflector membrane, and a tunable reflectance GMR grating is integrated on the diaphragm. Therefore, we set $R_1 = 0.99$ and $R_2 = 0.30.60.90.99$ as the input parameters for equation (5) to simulate the case of utilizing TRR and metal reflector, and the curves are shown in Fig. 13(a). $A'(L_0)$ is calculated by traversing L_0 over the entire period range and the working points are chosen where the maximum $A'(L_0)$ is located, as marked by black points and arrows in Fig. 13(b). The dynamic range was chosen according to the nonlinearity of the quasi-linear range, with a threshold of 5%, as given by Fig. 13(b). Detailed data on the dynamic range and sensitivity are given in Table V.
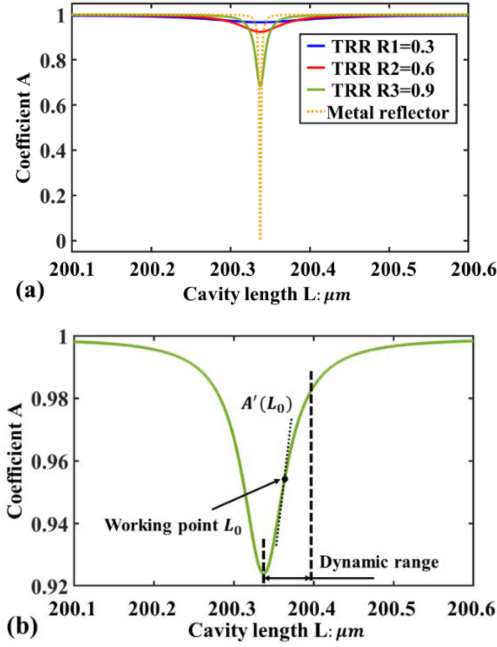
Fig. 13. (a) Calculated coefficient A versus cavity length using TRR with reflectance of $R_2 = 0.30.60.9$ and metal reflector with reflectance of $R_2 = 0.99$, $R_1 = 0.99$ is set to simulate that a metal reflector has been coated on the end face of fiber. (b) Illustration of defining working point (midpoint of quasi-linear range), dynamic range and $A'(L_0)$.

As can be seen from Table V, the sensitivity of the F-P sensor appears to be enhanced by two orders of magnitude according to equation (6), however, the dynamic range also decrease from $118nm$ to $13nm$. Herein, only three groups of reflectivity are used in the calculation, and considering the reflectivity tuning range of our GMR grating, more appropriate sensitivity and dynamic range may be achieved by carefully adjusting the reflectivity. Meanwhile, though $A'(L_0)$ can be improved to 64.603 by using metal reflector, however, the dynamic range is only $6nm$ and the performance of sensor can not be tuned due to constant reflectivity offered by metal reflector.

D. Spectrum-Based Peak-to-Peak Demodulation Method

The accuracy of the positioning apex in the spectrum is important in spectrum-based demodulation methods, especially in the peak-to-peak method. Generally, the accuracy of the locating apex can be influenced by both resolution of spectrometer and the fineness of spectrum, where the common point of both methods is to highlight the apex. The proposed GMR grating is also useful for spectrum-based demodulation methods because of its ability to significantly increase the fineness of the interference spectrum. This is especially useful for the peak-to-peak method for low fineness and brings uncertainty in determining the position of adjacent apexes, further resulting in the inaccurate determination of cavity length, as given by equation (7) [41]:

$$d = \frac{\lambda_1 \lambda_2}{2\Delta\lambda_{MN}} \quad (7)$$

where d is the length of the Fabry-Perot cavity, λ_1 and λ_2 are the locations of adjacent apexes in the spectrum, and $\Delta\lambda_{MN}$ is the wavelength spacing of adjacent apexes.
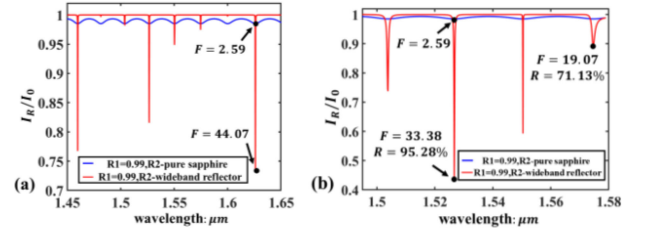

Fig. 14. Calculated reflectance spectrum of Fabry-Perot cavity formed by two mirrors of fiber end face and diaphragm with GMR grating, therein $R_1 = 0.99$ and R_2 equals the reflectance of GMR grating. (a) R_2 equals the reflectance of extrinsic WFR; (b) R_2 equals the reflectance of intrinsic WFR. The black points and arrows indicate the sampling points chosen to calculate the fineness.

Therefore, we compare the spectrum of the following two circumstances assuming that the end face of the fiber is coated with a metal reflector: $R_1 = 0.99$, $R_2 = 0.04$, and $R_1 = 0.99$. R_2 equals the reflectance of the WFR in its flat-top band, and the spectrum is calculated according to equations (4) and (5); the cavity length is therefore set to be $L = 50\mu m$, and the result is shown in Fig. 14.

For the convenience of quantitatively evaluating the result of utilizing the GMR grating, the fineness of a few troughs calculated using equation (8) are marked in the Fig. 14.

$$F = \frac{2\pi}{\Delta\delta} \quad (8)$$

Where F stands the fineness of spectrum and $\Delta\delta$ represents full width at half maximum of an apex. As can be seen, the fineness of the spectrum formed by the pure sapphire diaphragm and metal-coated fiber is approximately 2.59, while the maximum fineness of the GMR WFR is approximately 44.07. Therefore, the fineness of the apex can be greatly improved by integrating the GMR grating. Furthermore, considering that the high reflectance band of the intrinsic GMR reflector is less flat than that of the extrinsic GMR reflector, as illustrated in the previous section, the reflectance and fineness are marked together for the two apexes in Fig. 14(b).

VI. CONCLUSION

A sapphire-based GMR reflector for F-P sensors applied in harsh environments was proposed in this paper. The GMR reflector is separately designed for intensity-based and phase-based demodulation methods using the PSO algorithm with a target spectrum exhibiting a falling/rising edge or a flat-top high reflectance band, called TRR and WFR, respectively. Meanwhile, the GMR reflector is divided into extrinsic and intrinsic types by the material of scatter, and the optical properties and temperature resistance are investigated through numerical simulation approaches. For WFR, the extrinsic GMR grating shows R > 0.99 across the wavelength range of $1.45 - 1.65\ \mu m$, while the intrinsic GMR grating shows R > 0.85 across only a $78\ nm$ bandwidth in the wavelength range of $1.495 - 1.573\mu m$ owing to the low refractive index of sapphire. As for TRR, both extrinsic and intrinsic gratings exhibit available falling or rising edges with similar temperature resistances. In general, the extrinsic GMR grating is more suitable to be adopted for manipulating performance of sensor due to the strong optic control ability, however the temperature resistance of intrinsic GMR grating is

obviously higher than that of extrinsic GMR grating mainly due to absence of thermal stress brought by hetero-layers.

Finally, the sensitivity enhancement of a typical F-P sensor produced by our GMR reflector was investigated through the F-P interference model, and the results show that the sensitivity can be improved by two orders of magnitude while the dynamic range is decreased to the same level, and the optimized value of these two indexes can be found by tuning the reflectance of the reflector. In addition, the fineness of the spectrum can be promoted by one order of magnitude by adopting the GMR WFR, which could further improve the accuracy of positioning apexes for the phase-based peak-to-peak demodulation method. This indicates the excellent availability of our GMR reflector and its broad prospects in harsh-environment applications. This work can also be extended to research on weakly modulated GMR gratings using low-refractive-index materials and sapphire substrates used in GaN-based lasers.

REFERENCES

[1] M. Tahan, E. Tsoutsanis, M. Muhammad, and Z. Karim, "Performance-based health monitoring, diagnostics and prognostics for condition-based maintenance of gas turbines: A review," *Appl. Energy*, vol. 198, pp. 122–144, 2017.

[2] J. Yonggang, L. Jian, Z. Zhiwen, J. Xinggang, and Z. Deyuan, "Fabrication of All-SiC fiber-optic pressure sensors for high-temperature applications," *Sensors*, vol. 16, no. 10, 2016, Art. no. 1660.

[3] S. Pevec and D. Donlagic, "Miniature all-fiber Fabry-Perot sensor for simultaneous measurement of pressure and temperature," *Appl. Opt.*, vol. 51, no. 19, pp. 4536–4541, 2012.

[4] W. Li, T. Liang, P. Jia, C. Lei, and J. Xiong, "Fiber-optic Fabry–Perot pressure sensor based on sapphire direct bonding for high-temperature applications," *Appl. Opt.*, vol. 58, no. 7, 2019, Art. no. 1662.

[5] B. Griffin, D. Mills, T. Schmitz, and M. Sheplak, "A sapphire based fiber optic dynamic pressure sensor for harsh environments: Fabrication and characterization," in *Proc. Aiaa Aerosp. Sci. Meeting Including New Horiz. Forum Aerosp. Expo.*, 2010, Art. no. 2514.

[6] H. Zhou, D. A. Mills, A. Vera, A. Garraud, and M. Sheplak, "A high-temperature optical sapphire pressure sensor for harsh environments," in *Proc. AIAA Scitech 2019 Forum*, 2019, pp. 1–42.

[7] R. D. Pechstedt, "Fibre optic pressure and temperature sensor for applications in harsh environments," in *Proc. 5th Eur. Workshop Opt. Fibre Sensors*, 2013, Art. no. 879405.

[8] M. Palmer, M. Davis, G. Engelbrecht, R. Fielder, and A. Ringshia, "Un-Cooled fiber-optic pressure sensor for turbine engines," in *Proc. 44th AIAA Aerosp. Sci. Meeting Exhib.*, 2013, pp. 865–874.

[9] K. Kadirvel, R. Taylor, S. Horowitz, L. Hunt, and M. Sheplak, "Design and characterization of MEMS optical microphone for aeroacoustic measurement," in *Proc. 42nd AIAA Aerosp. Sci. Meeting Exhib.*, 2004, pp. 2–10.

[10] Z. Gong *et al.*, "High-Sensitivity Fabry-Perot interferometric acoustic sensor for low-frequency acoustic pressure detections," *J. Lightw. Technol.*, vol. 35, no. 24, pp. 5276–5279, Dec. 2017.

[11] J. Eom, C. J. Park, B. H. Lee, J. H. Lee, and E. Chung, "Fiber optic Fabry–Perot pressure sensor based on lensed fiber and polymeric diaphragm," *Sensors Actuators A Phys.*, vol. 225, pp. 25–32, 2015.

[12] S. E. Hayber, T. E. Tabaru, S. Keser, and O. G. Saracoglu, "A simple, high sensitive fiber optic microphone based on cellulose triacetate diaphragm," *J. Lightw. Technol.*, vol. 36, no. 23, pp. 5650–5655, Dec. 2018.

[13] P. Jia *et al.*, "Batch-producible MEMS fiber-optic Fabry-Perot pressure sensor for high-temperature application," *Appl. Opt.*, vol. 57, no. 23, pp. 6687–6692, 2018.

[14] L. Huang, D. Liang, J. Zeng, Y. Xiao, H. Wu, and W. Xiao, "A silicon-based wideband multisubpart profile grating reflector," *Opt. Laser Technol.*, vol. 78, pp. 79–82, 2016.

[15] H. Wu, L. Huang, Y. Xiao, C. Zhang, and Y. Gao, "A wideband reflector realized by a subwavelength multi-subpart profile grating structure," *J. Opt.*, vol. 15, no. 3, 2013, Art. no. 035703, pp. 4337–4340.

[16] R. Magnusson and M. Shokooh-Saremi, "Physical basis for wideband resonant reflectors," *Opt. Exp.*, vol. 16, no. 5, pp. 3456–3462, 2008.

[17] R. Magnusson, "Wideband reflectors with zero-contrast gratings," *Opt. Lett.*, vol. 39, no. 15, 2014.

[18] S.-S. Mehrdad and R. Magnusson, "Wideband leaky-mode resonance reflectors: Influence of grating profile and sublayers," *Opt. Exp.*, vol. 16, no. 22, pp. 18249–18263, 2008.

[19] M. M. Shokooh-Saremi1, "Leaky-mode resonant reflectors with extreme bandwidths," *Opt. Lett.*, vol. 35, no. 8, 2010, Art. no. 1121.

[20] O. Kilic, M. J. F. Digonnet, G. S. Kino, and O. Solgaard, "Miniature photonic-crystal hydrophone optimized for ocean acoustics," *J. Acoustical Soc. Amer.*, vol. 129, no. 4, pp. 1837–1850, 2011.

[21] O. Kilic, M. Digonnet, G. Kino, and O. Solgaard, "External fibre Fabry–Perot acoustic sensor based on a photonic-crystal mirror," *Meas. Sci. Technol.*, vol. 18, no. 10, 2007, Art. no. 3049.

[22] S. H. Kim and J. J. LEe, "Phase-shifted transmission/reflection-type hybrid extrinsic Fabry-Perot interferometric optical fiber sensors," *J. Lightw. Technol.*, vol. 21, no. 3, pp. 797–804, Mar. 2003.

[23] Y. Zhihao and A. Wang, "Fast demodulation algorithm for multiplexed low-finesse Fabry–Pérot interferometers," *J. Lightw. Technol.*, vol. 34, no. 3, pp. 1015–1019, Feb. 2016.

[24] B. Zhang, X. Tong, H. Pan, G. Qian, and C. Zhou, "Wavelet phase extracting demodulation algorithm based on scale factor for optical fiber Fabry-Perot sensing," *Opt. Exp.*, vol. 24, no. 26, pp. 29506, 2016.

[25] I. H. Malitson, F. V. Murphy, and W. S. Rodney, "Refractive index of synthetic sapphire," *J. Opt. Soc. Amer.*, vol. 48, no. 1, pp. 72–73, 1958.

[26] H. H. Li, "Refractive index of silicon and germanium and its wavelength and temperature derivatives," *J. Phys. Chem. Reference Data*, vol. 9, no. 3, pp. 561–658, 1980.

[27] K. Hotta, A. Yamaguchi, and N. Teramae, "Nanoporous waveguide sensor with optimized nanoarchitectures for highly sensitive label-free biosensing," *ACS Nano*, vol. 6, no. 2, pp. 1541–1547, 2012.

[28] A. K. Kodali, M. Schulmerich, J. Ip, G. Yen, B. T. Cunningham, and R. Bhargava, "Narrowband midinfrared reflectance filters using guided mode resonance," *Anal. Chem.*, vol. 82, no. 13, pp. 5697–5706, 2010.

[29] S. G. Kaplan and M. E. Thomas, "Measurement of the o-ray and e-ray infrared refractive index and absorption coefficient of sapphire from 10 K to 295 K," in *Proc. Int. Symp. Opt. Sci. Technol.*, 2002, Art. no. 451770.

[30] N. Papasimakis, V. A. Fedotov, V. Savinov, T. A. Raybould, and N. I. Zheludev, "Electromagnetic toroidal excitations in matter and free space," *Nature Mater.*, vol. 15, no. 3, pp. 263–271, 2016.

[31] A. A. Bogdanov *et al.*, "Bound states in the continuum and fano resonances in the strong mode coupling regime," *Adv. Photon.*, vol. 1, no. 1, 2019, Art. no. 016001.

[32] H. Heo, S. Lee, and S. Kim, "Tailoring fano resonance for flat-top broadband reflectors based on single guided-mode resonance," *J. Lightw. Technol.*, vol. 37, no. 17, pp. 4244–4250, Sep. 2019.

[33] D. Yang, M. E. Thomas, and S. G. Kaplan, "Measurement of the infrared refractive index of sapphire as a function of temperature," in *Proc. Conf. Window Dome Technol. Mater. VII*, 2001, pp. 53–63.

[34] G. E. Jellison and H. H. Burke, "The temperature dependence of the refractive index of silicon at elevated temperatures at several laser wavelengths," *J. Appl. Phys.*, vol. 60, no. 2, pp. 841–843, 1986.

[35] E. R. Dobrovinskaya, L. A. Lytvynov, and V. Pishchik, *Sapphire: Material, Manufacturing, Applications*, New York, NY, USA: Springer, 2009.

[36] S. Uma, A. D. McConnell, M. Asheghi, K. Kurabayashi, and K. E. Goodson, "Temperature-dependent thermal conductivity of undoped polycrystalline silicon layers," *Int. J. Thermophysics*, vol. 22, no. 2, pp. 605–616, 2001.

[37] H. TaDa *et al.*, "Thermal expansion coefficient of polycrystalline silicon and silicon dioxide thin films at high temperatures," *J. Appl. Phys.*, vol. 87, no. 9, pp. 4189–4193, 2000.

[38] H. R. Shanks, P. D. Maycock, P. H. Sidles, and G. C. Danielson, "Thermal conductivity of silicon from 300 to 1400°K," *Phys. Rev.*, vol. 130, no. 5, pp. 1743–1748, 1963.

[39] H. Aida, T. Doi, H. Takeda, H. Katakura, and M. Uneda, "Ultraprecision CMP for sapphire, GaN, and SiC for advanced optoelectronics materials," *Curr. Appl. Phys.*, vol. 12, no. 9, pp. S41–S46, 2012.

[40] D.-J. Kang *et al.*, "Inductively coupled plasma reactive ion etching of sapphire using C2F6- and NF3-based gas mixtures," *Mater. Sci. Semicond. Process.*, vol. 11, no. 1, pp. 16–19, 2008.

[41] Y. Jiang, "High-resolution interrogation technique for fiber optic extrinsic Fabry-Perot interferometric sensors by the peak-to-peak method," *Appl. Opt.*, vol. 47, no. 7, pp. 925–932, 2008.